Research Square

Preprints are preliminary reports that have not undergone peer review.
They should not be considered conclusive, used to inform clinical practice,
or referenced by the media as validated information.

Influence of the high-melting-point solder addition on the thermo-mechanical reliability of solderable anisotropic polymer composites containing low-melting-point solder

Yi Hyeon Baek
Chung-Ang University
Jong-Min Kim
Chung-Ang University
Byung-Seung Yim
bsyim@kangwon.ac.kr
Kangwon National University

Research Article

Keywords: Anisotropic conductive adhesive, High-melting-point solder, Low-melting-point solder, Solderable anisotropic polymer composites, Thermo-mechanical reliability

Posted Date: September 2nd, 2026

DOI: https://doi.org/10.21203/rs.3.rs-10798017/v1

License: This work is licensed under a Creative Commons Attribution 4.0 International License.
Read Full License

Additional Declarations: No competing interests reported.

Version of Record: A version of this preprint was published at Journal of Materials Science: Materials in Electronics on October 23rd, 2026. See the published version at https://doi.org/10.1007/s10854-026-18747-y.

Abstract

To examine how adding a high-melting-point solder (HMS) filler affects the thermo-mechanical reliability of a low-melting-point solder (LMS)-based solderable anisotropic polymer composite (SAPC), L-SAPC (LMS only) and LH-SAPC (LMS/HMS) were synthesized and subjected to thermal shock testing (–55 to 125°C, 1000 cycles). LH-SAPC exhibited superior initial mechanical bonding compared to L-SAPC, attributed to precipitation hardening and dispersion strengthening from fine Cu_6Sn_5, Ag_3Sn, and Bi-rich phase particles within the conduction paths. Both SAPCs maintained stable electrical reliability throughout thermal shock testing, due to the formation of a stable metallurgical conduction path. Although both SAPCs showed reduced pull strength after thermal cycling, LH-SAPC outperformed L-SAPC in thermo-mechanical reliability, due to stronger initial bonding from the LMS/HMS filler, reduced microstructural coarsening, slower interfacial intermetallic compound (IMC) growth and flattening, and less Bi-rich phase accumulation at the bulk solder/Cu_6Sn_5 IMC interface.

1 Introduction

With the growing integration, performance, and miniaturization of semiconductor packages driven by advances in information and communications technology, electronic package joints have become increasingly susceptible to thermo-mechanical reliability issues [1, 2]. Electronic packages, composed of materials with mismatched coefficients of thermal expansion (CTEs), experience thermal and power stress that causes joint cracking, delamination, and thermal fatigue from repeated expansion and contraction, which directly affect the electronic package functionality [3–5]. Thus, thermo-mechanical reliability is a critical consideration in electronic packaging [6]. Conventional anisotropic conductive adhesives (ACAs), comprising fine metal particles dispersed in a thermosetting polymer resin, establish selective vertical conduction paths between matching electrodes. Due to their anisotropic properties, these materials eliminate the need for a separate underfill process, provide full-area bonding, enable low-temperature processing, streamline manufacturing, and facilitate ultra-fine pitch bonding using conductive particles with a few μm in diameter [7, 8]. However, commercial ACAs remain susceptible to increased contact resistance under harsh environments (e.g., thermal cycling or high-temperature/high-humidity exposure), as their conduction relies on physical contact between non-fusible metal fillers and corresponding electrodes, while mechanical stability depends solely on cured polymer restraint. Furthermore, moisture absorption and degradation may weaken adhesion, potentially causing interfacial delamination and consequent loss of electrical connectivity [9, 10]. To overcome these limitations, solderable anisotropic polymer composites (SAPCs) incorporating fusible low-melting-point solder (LMS) filler and a reducing polymer matrix were developed [11–13]. During reflow, SAPCs form metallurgical conduction paths via molten LMS coalescence and selective wetting on electrodes, with mechanical reinforcement provided by the cured polymer surrounding the conduction path. Through this metallurgical conduction formation, SAPCs achieve superior electrical stability and mechanical bonding compared to conventional ACAs, while retaining benefits of commercial ACA (e.g., low-temperature processing and process simplicity). To enable proper conduction path formation, SAPCs require an LMS

filler with a melting point below the polymer curing temperature. Thus, Sn–58Bi eutectic solder (melting temperature ~ 139°C) is used as the LMS filler. However, SAPC joints using Sn–58Bi solder are prone to reliability issues, including brittleness and coarsening of the Bi-rich phase, excessive intermetallic compound (IMC) growth, and Bi segregation at the joint interface [14–16].

To resolve the above issues with Sn–58Bi-based SAPCs, our research group proposed a novel LH-SAPC system incorporating mixed LMS/high-melting-point solder (HMS) fillers (Fig. 1) [17, 18]. During reflow, molten LMS coalesces within the low-viscosity polymer into large spherical fillers, while solid HMS fillers are absorbed upon contact with the coalesced LMS. Subsequently, selective wetting of the LMS filler, now containing solid HMS particles, onto the electrodes forms metallurgical conduction paths between the opposing upper and lower electrodes. As reflow proceeds, polymer curing initiates, and upon reaching the melting point of the entrapped HMS fillers, they melt and form a solid solution with LMS within the conduction path. Finally, complete curing of the surrounding polymer matrix solidifies the joint structure.

In this study, L-SAPC (LMS only) and LH-SAPC (LMS/HMS) assemblies were prepared, and subjected to thermal shock testing to evaluate the thermo-mechanical reliability of the mixed-filler joints.

Figure 1

2 Experimental

2.1 Materials

The SAPCs employed in this study comprise a reductively functionalized polymer matrix and a fusible solder filler to establish electrical, mechanical, and metallurgical interconnections (Table 1). The polymer composite was synthesized using a thermosetting diglycidyl ether of bisphenol A (DGEBA, Kukdo Chemical, Korea) as the base resin, 4,4'-diaminodiphenylmethane (DDM, TCI Korea Co., Korea) as the curing agent, and boron trifluoro-mono-ethylamine (BF_3MEA, Sigma-Aldrich, USA) as the catalyst. Carboxylic acid (Sigma-Aldrich, USA) was additionally employed as a reducing agent to eliminate surface oxides on both the solder filler and electrodes during reflow. Sn–58Bi (melting point ~ 139°C) and Sn–3.0Ag–0.5Cu (melting point ~ 219°C) solder powders (Danyang Soltech, Korea) have an average particle size of 38 μm.

A thin quad flat package (TQFP, TQFP44T30, Topline Co., USA) and a printed circuit board (PCB) were used to fabricate the thermal shock test specimens. The TQFP measured 12 × 12 × 1.2 mm^3, with 11 Sn-plated Cu leads per side at a 0.8 mm pitch. The PCB, measuring 32 × 32 × 1.0 mm^3, featured bare Cu electrodes (no surface finish) plated to a thickness of 18 μm. A daisy-chain was incorporated into both the TQFP and PCB to monitor electrical performance changes in the LH-SAPC during reliability testing.

Table 1
Constituent materials of the proposed SAPCs.

Components		L-SAPC	LH-SAPC
Polymer composite	Base resin	DGEBA	
	Curing agent	DDM	
	Catalyst	BF3MEA	
	Reductant	Carboxylic acid	
Solder filler	LMS	Sn–58Bi (φ 38 μm)	
	HMS	Sn–3Ag–0.5Cu (φ: 38 μm)	
	LMS/HMS mixing ratio (vol%)	100:0	50:50

Table 1

2.2 Test method

2.2.1 Preparation of test specimens

To examine the influence of LMS/HMS filler incorporation on thermo-mechanical reliability, two SAPC variants were synthesized: L-SAPC (with LMS filler only) and LH-SAPC (with an LMS/HMS filler mixture at a 50:50 volume ratio (vol%)). Due to their anisotropic conduction behavior, which enables selective path formation to the electrodes, SAPCs are applied over the entire joint area, including both the electrode and PCB regions. Accordingly, to achieve broad and stable conduction paths on the electrodes while preventing short-circuits between adjacent electrodes, the solder filler content in the SAPC was kept relatively low at 15 vol%. Following synthesis of the L-SAPC and LH-SAPC, TQFP bonding was conducted to prepare thermal shock test specimens. A 100-μm-thick metal mask was aligned and mounted on the cleaned PCB, and the SAPC pastes were uniformly applied to the exposed joint region using a squeegee. Subsequently, the TQFP leads were aligned with the PCB electrodes and mounted using a flip chip bonder (LAMBDA, Finetech Co., Germany), followed by reflow according to the reflow profile in Fig. 2. The L-SAPC specimen was heated from room temperature to 180°C at 120°C min^{-1} to enable LMS melting and wetting, then held for ~ 2 min to cure the polymer (reflow profile 1). Conversely, the LH-SAPC specimen was heated from room temperature to 240°C to completely melt the HMS filler, followed by a 2 min hold at peak temperature to complete TQFP bonding (reflow profile 2). Following TQFP bonding, the SAPC assemblies were epoxy-molded, cross-sectioned, and examined under an optical microscope (VHX-1000, Keyence Co., Japan) to observe conduction path morphologies.

Figure 2

2.2.2 Thermal shock reliability test

To investigate the effect of LMS/HMS filler on the thermo-mechanical reliability, thermal shock testing was performed using a thermal shock chamber (TSE-11-A, Espec Co., Japan). Thermal shock testing was performed for 1000 cycles under repetitive thermal fluctuation of − 55 to 125°C in accordance with JEDEC standard JESD22-A106B condition C. Holding time at each extreme was 15 min, with a transition of 10 s and ramp rate of ~ 18°C s^{-1}.

During thermal shock testing, the electrical resistance of the SAPC assemblies was monitored using a multimeter (34410A, Agilent Tech, USA) to evaluate changes in joint electrical performance. To confirm mechanical performance changes during thermal shock testing, a 45° pull test was performed on the TQFP joint at selected cycles using a pull tester (PTR-1000, Rhesca Co., Japan). The specimen was secured on a 45°-tilted stage, and pull strength was measured by pull testing the TQFP leads at a pull speed of 6 mm/min, following JEDEC standard JIS Z 3198-6.

2.2.3 Microstructure and fracture mode analyses

To determine the underlying causes of mechanical property changes in the SAPC joint following thermal shock testing, microstructure and fracture mode analyses were conducted. To evaluate microstructural evolution and IMC layer growth behavior at the bulk solder/electrode interface during thermal shock testing, SAPC assemblies subjected to selected cycles (0, 200, 500, and 1000) were epoxy-molded, then grinded and polished using silicon carbide paper and 3 μm diamond suspension. The specimens were then etched for ~ 10 s in a methanol–nitric acid solution (90:10 wt%) to clearly delineate the microstructure and IMC phase boundaries. Microstructural and IMC morphological changes within the SAPC joint were examined using a field emission scanning electron microscope (FE-SEM, JSM-7001F, JEOL Ltd., Japan) in backscattered electron (BSE) mode, while phase compositions were identified via energy dispersive X-ray spectroscopy (EDS, X-MaxN, Oxford Instruments Co., England). Additionally, fracture surface analysis of the pulled joints was conducted using FE-SEM and EDS to examine changes in fracture characteristics as a function of thermal shock cycling.

3 Results and discussion

3.1 Thermo-mechanical reliability of the SAPC joints

To measure the effect of LMS/HMS filler addition on thermo-mechanical reliability, TQFP assemblies fabricated with L-SAPC and LH-SAPC were subjected to thermal shock testing. Conduction path morphologies before testing are presented in Fig. 3. Each SAPC joint comprised a solder-filled conduction path between the TQFP lead and the electrode, surrounded by a cured polymer composite region (outer boundary indicated by a dotted line). The cured polymer composite region surrounding the conduction path serves to shield it from environmental factors and enhance the mechanical integrity of the SAPC joint. As observed, both SAPC joints formed broad, stable metallurgical conduction paths between the lead and the electrode. In the L-SAPC joint (Fig. 3(a)), the conduction path resulted from LMS filler flow, coalescence of adjacent molten LMSs within the low-viscosity polymer, and selective wetting of coalesced LMS onto the electrode. Conversely, as mentioned earlier, the LH-SAPC conduction

path (Fig. 3(b)) was formed when the coalesced molten LMS containing solid HMS particles selectively wetted the electrodes within the still-low-viscosity polymer composite. Final joint formation was completed via solid-solution conduction paths, achieved through melting of the solid HMS fillers as temperature increased, followed by full curing of the polymer composite [17–19]. These results confirm that both SAPCs formed conduction paths of comparable areas; thus, any influence of path size on reliability may be considered negligible.

The electrical resistance of both SAPC assemblies remained constant at ~ 2 Ω throughout the thermal shock test, indicating consistent electrical performance (Fig. 4). Electrical resistance in electronic devices can significantly increase when damage reduces the effective joint area (e.g., crack propagation or interfacial delamination). Thus, the stable electrical resistance of SAPC assemblies indicates that the conduction path remained structurally stable, without cracking or degradation, under rapid and repeated thermal cycling. These results confirm that SAPC joints can ensure stable electrical reliability under thermal shock, regardless of HMS filler addition, due to the formation of wide, stable metallurgical conduction paths.

The thermo-mechanical reliability of both SAPC joints was evaluated via a 45° pull test on TQFP assemblies during thermal shock testing (Fig. 5). Before the thermal shock testing, the LH-SAPC joint's initial pull strength (18.064 ± 0.595 N) improved by ~ 33.36% compared to the L-SAPC joint (13.546 ± 1.005 N). As reported previously [17, 18], this mechanical improvement in LH-SAPC joints is attributed to compositional and microstructural changes in the conduction path resulting from the LMS/HMS filler system. With HMS filler addition, the total Sn composition in the LH-SAPC solder increases, shifting the LMS filler from a eutectic (i.e., Sn–58Bi) to a hypo-eutectic composition. During solidification, fine IMCs (Cu_6Sn_5, Ag_3Sn) form via Sn–Cu/Ag reactions, and as cooling proceeds below the liquidus, primary Sn phases precipitate. As cooling continues below the LMS eutectic isotherm, fine Bi-rich phases precipitate due to a reduced Bi solubility in the Sn matrix. This altered solidification mechanism results in fine Cu_6Sn_5, Ag_3Sn, and Bi-rich phase particles uniformly distributed throughout the conduction path. Thus, through precipitation hardening and dispersion strengthening from these fine phases, LH-SAPC joints exhibit greater mechanical bonding strength than L-SAPC. As thermal shock cycling progressed, the mechanical pull strength of both SAPC joints gradually decreased from their initial pull values. This decrease is attributable to the excessive growth and flattening of the interfacial IMC layer, along with microstructural coarsening in the conduction path, driven by accelerated atomic diffusion under thermal cycling [20–22]. Despite declining from its initial value, LH-SAPC maintained superior mechanical properties over L-SAPC throughout thermal shock testing due to the higher initial bond strength from the LMS/HMS solidification mechanism. After thermal shock testing, the LH-SAPC joint exhibited ~ 46.91% higher pull strength than L-SAPC, confirming that LMS/HMS fillers enhance the thermo-mechanical reliability of SAPC joints.

Figure 3

Figure 4

Figure 5

3.2 Microstructure and fracture mode analyses

To identify the cause of LH-SAPC's improved thermo-mechanical reliability, microstructural analysis of the conduction paths was performed (Fig. 6). Prior to thermal shock testing, the L-SAPC joint exhibited a lamellar eutectic structure with alternating Sn-rich and Bi-rich phases [23]. In contrast, the LH-SAPC joint, due to the high-Sn HMS filler, did not form a lamellar structure; instead, it developed a microstructure with fine IMCs (Cu_6Sn_5, Ag_3Sn) and a Bi-rich phase uniformly dispersed within a wide Sn-rich matrix. As noted, these finely dispersed phases within the conduction path inhibit dislocation movement and localized plastic deformation, enhancing the joint's mechanical properties [17, 18].

During thermal shock testing, the initial lamellar eutectic structure in the L-SAPC joint gradually disappeared due to phase coarsening. In contrast, the LH-SAPC joint also exhibited progressive coarsening of fine particle phases (Cu_6Sn_5 and Ag_3Sn IMCs, and Bi-rich phase) with increasing cycles. However, its coarsening rate was notably lower than that observed for L-SAPC.

Microstructural coarsening in solder joints is accelerated by thermal energy at elevated temperatures and mechanical energy from repetitive or static stresses. High-temperature exposure enhances atomic diffusion, accelerating microstructural coarsening. Mechanical stress also promotes coarsening by inducing plastic deformation, which generates dislocations and vacancies that act as additional diffusion pathways, further accelerating phase coarsening. [24–26]. Thus, the reduced microstructural coarsening in LH-SAPC joints during thermal shock may be attributed to the improved mechanical bonding from LMS/HMS fillers, which limits plastic deformation and suppresses additional atomic diffusion.

Figure 7 illustrates the evolution of interfacial IMC layer morphologies at the conduction path/Cu electrode interface in SAPC joints during the thermal shock testing. Immediately after reflow, a dense scallop-shaped Cu_6Sn_5 IMC layer formed at the bonding interface due to the reaction between the electrode Cu and the solder Sn ($6Cu + 5Sn \rightarrow Cu_6Sn_5$) [27, 28]. In L-SAPC, the initial Cu_6Sn_5 IMC layer measured 1.234 ± 0.503 μm thick, with a Bi-rich phase accumulating at parts of the bulk solder/Cu_6Sn_5 IMC interface due to Sn consumption during IMC formation [29]. In LH-SAPC, the initial Cu_6Sn_5 IMC layer was thicker (1.905 ± 0.844 μm) than that in L-SAPC, due to the high reflow peak temperature (reflow profile 2) required to melt the HMS filler.

During thermal shock, the IMC layer thickness in both joints gradually increased, and a Cu_3Sn IMC layer additionally formed between the Cu_6Sn_5 IMC and Cu electrode via interatomic solid-state reactions ($3Cu + Sn \rightarrow Cu_3Sn$; $9Cu + Cu_6Sn_5 \rightarrow 5Cu_3Sn$) [27, 28]. In L-SAPC, the Cu_6Sn_5 IMC layer increased rapidly with cycling, transitioning from a thin scalloped to a thick flattened morphology. This morphology change is attributed to faster Cu_6Sn_5 growth through the valleys between adjacent scallops, where diffusion distances are shorter than at the scallop tops [30]. Rapid Sn consumption from Cu_6Sn_5 growth led to

substantial Bi-rich phase accumulation at the bulk solder/IMC layer interface in L-SAPC joints. In contrast, despite the initially thicker Cu_6Sn_5 IMC layer in the LH-SAPC joint due to its higher reflow peak temperature, its growth during thermal shock cycling was lower than that of the L-SAPC joint. Consequently, the LH-SAPC joint exhibited a thinner IMC layer after testing (mean thickness after thermal shock test: 3.172 ± 0.574 μm and 4.034 ± 0.516 μm for LH-SAPC and L-SAPC, respectively). Furthermore, the IMC layer in the LH-SAPC joint exhibited less morphological flattening than that in the L-SAPC joint, preserving its scalloped structure. This reduced planarization is attributed to Ag_3Sn IMC particles existing between the bulk solder and the Cu_6Sn_5 IMC layer. As can be seen in Fig. 7, Ag_3Sn IMC particles located in the Cu_6Sn_5 IMC scallop valleys act as diffusion barriers, hindering Cu and Sn interdiffusion and thus suppressing IMC morphological change and thickness growth [31]. The higher Sn and lower Bi content in the LMS/HMS conduction path reduced Bi-rich phase accumulation at the bulk solder/Cu_6Sn_5 IMC interface.

Figure 8 illustrates the interfacial IMC thickness and growth rate during thermal shock. Figure 8(a) shows that IMC layer thickness increased with thermal shock cycles for both SAPC joints. As noted, the initial IMC layer of LH-SAPC was thicker than that of L-SAPC, attributed to the higher reflow peak temperature accelerating atomic diffusion. Despite a thicker initial IMC layer, LH-SAPC exhibited slower IMC growth during thermal shock, and became thinner than L-SAPC after ~ 200 cycles. L-SAPC showed a rapid growth rate (~ 226.9% relative to the initial thickness), whereas LH-SAPC showed a lower and gradual growth (~ 66.5%) with increasing thermal shock cycles (Fig. 8(b)).

The interfacial IMC layer, formed by elemental diffusion and chemical reactions between solder and electrode materials, is essential for achieving robust metallurgical bonding and ensuring electrical and mechanical reliability in the electronic joints. However, excessive IMC growth can cause brittle fracture from interfacial stress concentration, driven by IMC brittleness and property mismatches (e.g., CTE, elastic modulus, hardness) among solder, IMCs, and metallization, degrading mechanical performance, lifespan, and joint reliability [32–34]. Morphological changes from the IMC growth affect solder-joint reliability. The scallop-shaped IMC layer at the bulk solder/electrode interface may help distribute stress and suppress crack propagation, ensuring mechanical bonding and thermo-mechanical reliability. However, flattening of the IMC layer reduces shear resistance, making cracks propagate more easily than with scalloped IMC, thus accelerating mechanical degradation and shortening joint lifespan [35, 36]. Additionally, the Bi-rich phase accumulated at the flattened Cu_6Sn_5 IMC interface in L-SAPC (Fig. 6) reduces joint strength due to Bi brittleness [37].

Figure 9 demonstrates the fracture surface morphologies of both SAPC joints before and after thermal shock testing. Before thermal shock, the L-SAPC fracture surface (Fig. 9(a)) consisted of Sn-rich and Bi-rich phases with limited Cu_6Sn_5 grains, exhibiting ductile fracture through the bulk solder interior. After thermal shock, the L-SAPC fracture surface (Fig. 9(b)) remained in the bulk solder, but exhibited a semi-brittle mode with a notably larger Bi-rich phase area across the entire surface. As depicted in Fig. 7, this fracture mode change in L-SAPC resulted from Cu_6Sn_5 IMC planarization and increased Bi-rich phase

accumulation at the bulk solder/IMC interface. Cracks propagated within the Bi-rich phase and along the flattened IMC interface. In contrast, the LH-SAPC fracture surface before thermal shock (Fig. 9(c)) exhibited a ductile-brittle mixed mode with a larger Cu_6Sn_5 IMC area than L-SAPC. In this fracture mode, the crack propagated through the bulk solder/Cu_6Sn_5 IMC boundary and the interior of the Cu_6Sn_5 layer, reflecting improved mechanical properties in the LH-SAPC joint due to the LMS/HMS filler [38]. After thermal shock, the LH-SAPC fracture surface (Fig. 9(d)) exhibited a ductile-brittle mixed mode with bulk solder and Cu_6Sn_5 IMC, similar to before the thermal shock testing, despite some reduction in mechanical properties due to microstructural coarsening.

These results confirm that LH-SAPC offers improved thermo-mechanical reliability over L-SAPC, attributed to enhanced initial bonding from LMS/HMS fillers, reduced IMC growth and flattening, reduced microstructural coarsening, and decreased Bi-rich phase accumulation at the bulk solder/Cu_6Sn_5 interface.

Figure 6

Figure 7

Figure 8

Figure 9

4 Conclusions

To investigate the effect of LMS/HMS filler addition on SAPC joint thermo-mechanical reliability, two formulations, L-SAPC (LMS only) and LH-SAPC (LMS/HMS), were synthesized and subjected to thermal shock testing. LH-SAPC exhibited higher initial mechanical bonding strength than L-SAPC, attributed to precipitation hardening and dispersion strengthening from finely distributed Cu_6Sn_5, Ag_3Sn, and Bi-rich particles within the conduction paths. Both SAPCs maintained stable electrical reliability throughout thermal shock testing, due to the formation of a stable metallurgical conduction path. While mechanical pull strengths of SAPC assemblies decreased during thermal shock testing, LH-SAPC exhibited superior thermo-mechanical reliability over L-SAPC. This reliability improvement is attributed to the enhanced initial bond strength from the LMS/HMS filler, suppressed bond microstructure coarsening, reduced IMC layer growth and flattening, and less Bi-rich phase accumulation at the bulk solder/Cu_6Sn_5 IMC interface. The results confirm that LMS/HMS filler enhances both the initial bonding properties and thermo-mechanical reliability of the SAPC system.

Declarations

Conflict of interest

The authors declare no known competing financial interests or personal relationships that can influence the work reported in this paper.

Funding

This research did not receive any specific grant from funding agencies in the public, commercial, or not-for-profit sectors.

Author Contribution

YHB: conceptualization, methodology, investigation and writing the original draft; JMK: supervision and validation; BSY: supervision and validation.

Acknowledgments

This research was supported by Basic Science Research Program through the National Research Foundation of Korea (NRF) funded by the Ministry of Education (No. RS-2024-00414450)

Data availability

The datasets used or analyzed in this study are available with the corresponding author. They can be produced upon reasonable request.

References

1. N. Jiang, L. Zhang, Z.Q. Liu, L. Sun, W.M. Long, P. He, M. Zhao, Sci. Technol. Adv. Mater. **20**, 876–901 (2019)
2. Y. Yao, Y. An, J. Dong, Y. Wang, K.N. Tu, Y. Liu, J. Mater. Res. Technol. **31**, 3374–3382 (2024)
3. N.M. Poon, C.L. Wu, J.K. Lai, Y.C. Chan, IEEE Trans. Adv. Package. **23**, 708–714 (2002)
4. L. Zhang, S.B. Xue, L.L. Gao, Z. Sheng, S.L. Yu, Y. Chen, Z. Guang, Microelectron. Reliab. **50**, 2071–2077 (2010)
5. W.W. Lee, L.T. Nguyen, G.S. Selvaduray, Microelectron. Reliab. **40**, 231–244 (2000)
6. W. Ning, C. Zhu, H. Li, G. Xu, L. Luo, H. Guo, F. Jing, Mater. Sci. Semicond. Process. **16**, 933–939 (2013)
7. R. Aradhana, S. Mohanty, S.K. Nayak, Int. J. Adhes. Adhes. **99**, 102596 (2020)
8. Y. Li, C.P. Wong, Mater. Sci. Eng. R: Rep. **51**, 1–35 (2006)
9. Y. Guan, X. Chen, F. Li, H. Gao, Int. J. Adhes. Adhes. **30**, 80–88 (2010)

10. R. Dudek, H. Berek, T. Fritsch, B. Michel, IEEE Trans. Compon. Packag Technol. **23**, 462–469 (2000)
11. B.S. Yim, J.M. Kim, S.H. Jeon, S.H. Lee, J. Kim, J.G. Han, Y.S. Eom, Y.E. Shin, Mater. Trans. **50**, 1684–1689 (2009)
12. B.S. Yim, J.M. Kim, J. Mater. Sci. : Mater. Electron. **26**, 4969–4980 (2015)
13. B.S. Yim, Y.E. Shin, J.M. Kim, Microelectron. Reliab. **91**, 201–212 (2018)
14. W.U. Ping, Trans. Nonferr Met. Soc. China. **25**, 1225–1233 (2015)
15. F. Wang, Y. Huang, Z. Zhang, C. Yan, Mater. **10**, 920 (2017)
16. A.K. Gain, L. Zhang, J. Mater. Sci. Mater. Electron. **27**, 781–794 (2016)
17. M.J. Ha, J.I. Lee, J.M. Kim, B.S. Yim, J. Mater. Sci. : Mater. Electron. **34**, 890 (2023)
18. Y.H. Ha, J.I. Lee, J.M. Kim, B.S. Yim, J. Mater. Sci. : Mater. Electron. **35**, 2052 (2024)
19. M.J. Ha, J.I. Lee, J.M. Kim, B.S. Yim, J. Mater. Sci. : Mater. Electron. **34**, 1888 (2023)
20. B.S. Yim, J.M. Kim, J. Mater. Sci. Mater. Electron. **27**, 9159–9171 (2016)
21. T. An, F. Qin, Microelectron. Reliab. **54**, 932–938 (2014)
22. M. Shang, C. Li, Y. Wang, X. Chen, Y. Zhao, J. Ke, J. Chen, J. Mater. Res. Technol. **33**, 6307–6318 (2024)
23. N. Zhao, Y. Zhong, M.L. Huang, H.T. Ma, W. Dong, Sci. Rep. **5**, 13491 (2015)
24. J.D. Robson, Metall. Mater. Trans. A **51**, 5401–5413 (2020)
25. Y. Tian, N. Ren, Z. Zhao, F. Wu, S.K. Sitaraman, Materials. **11**, 2509 (2018)
26. H. Conrad, Z. Gui, Y. Fahmy, D. Yang, J. Electron. Mater. **28**, 1062–1070 (1999)
27. F. Wang, H. Chen, Y. Huang, C. Yan, J. Mater. Sci. : Mater. Electron. **29**, 11409–11420 (2018)
28. M.Y. Xiong, L. Zhang, J. Mater. Sci. **54**, 1741–1768 (2019)
29. Q.S. Zhu, Z.F. Zhang, Z.G. Wang, J.K. Shang, J. Mater. Res. **23**, 78–82 (2008)
30. R. Tian, C. Hang, Y. Tian, L. Zhao, Mater. Sci. Eng: A **709**, 125–133 (2018)
31. Y.A. Shen, Y.T. Tai, Y.T. Fang, C.H. Liu, N.T. Tsou, F.Y. Ouyang, H. Nishikawa, J. Mater. Sci. : Mater. Electron. **36**, 1183 (2025)
32. X. Wang, L. Zhang, X. Wang, Y.H. Guo, L. Sun, Y.X. Liu, X. Lu, J. Mater. Res. Technol. **21**, 4263–4280 (2022)
33. A. Jalar, M.A. Bakar, R. Ismail, A.R. Daud, J. Sci. Res. Dev. **3**, 49–54 (2016)
34. J.W. Yoon, S.B. Jung, J. Alloys Compd. **359**, 202–208 (2003)
35. P.L. Tu, Y.C. Chan, J.K.L. Lai, IEEE Trans. Compon. Packag Manuf. Technol. B **20**, 87–93 (2002)
36. Y.C. Chan, P.L. Tu, A.C. So, J.K.L. Lai, IEEE Trans. Compon. Packag Manuf. Technol. B **20**, 463–469 (2002)
37. Q. Zhang, H. Zou, Z.F. Zhang, J. Mater. Res. **25**, 303–314 (2010)
38. R. Sayyadi, H. Nafakh-Moosavy, Sci. Rep. **9**, 8389 (2019)

Figures

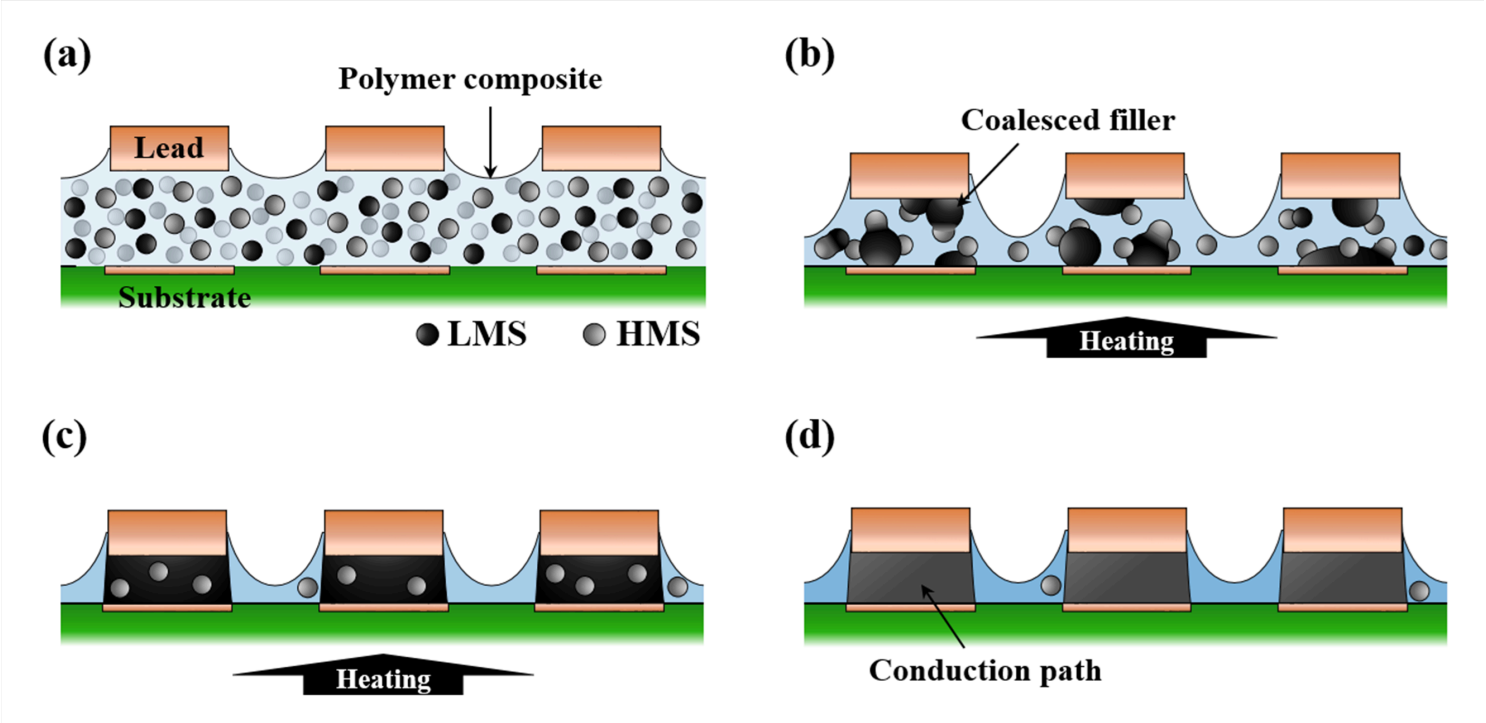


Figure 1

Conduction path formation in LH-SAPC: (a) initial condition, (b) molten LMS coalescence and HMS incorporation, (c) path formation on electrodes via selective wetting and polymer curing onset, and (d) solid-solution path after HMS melting.

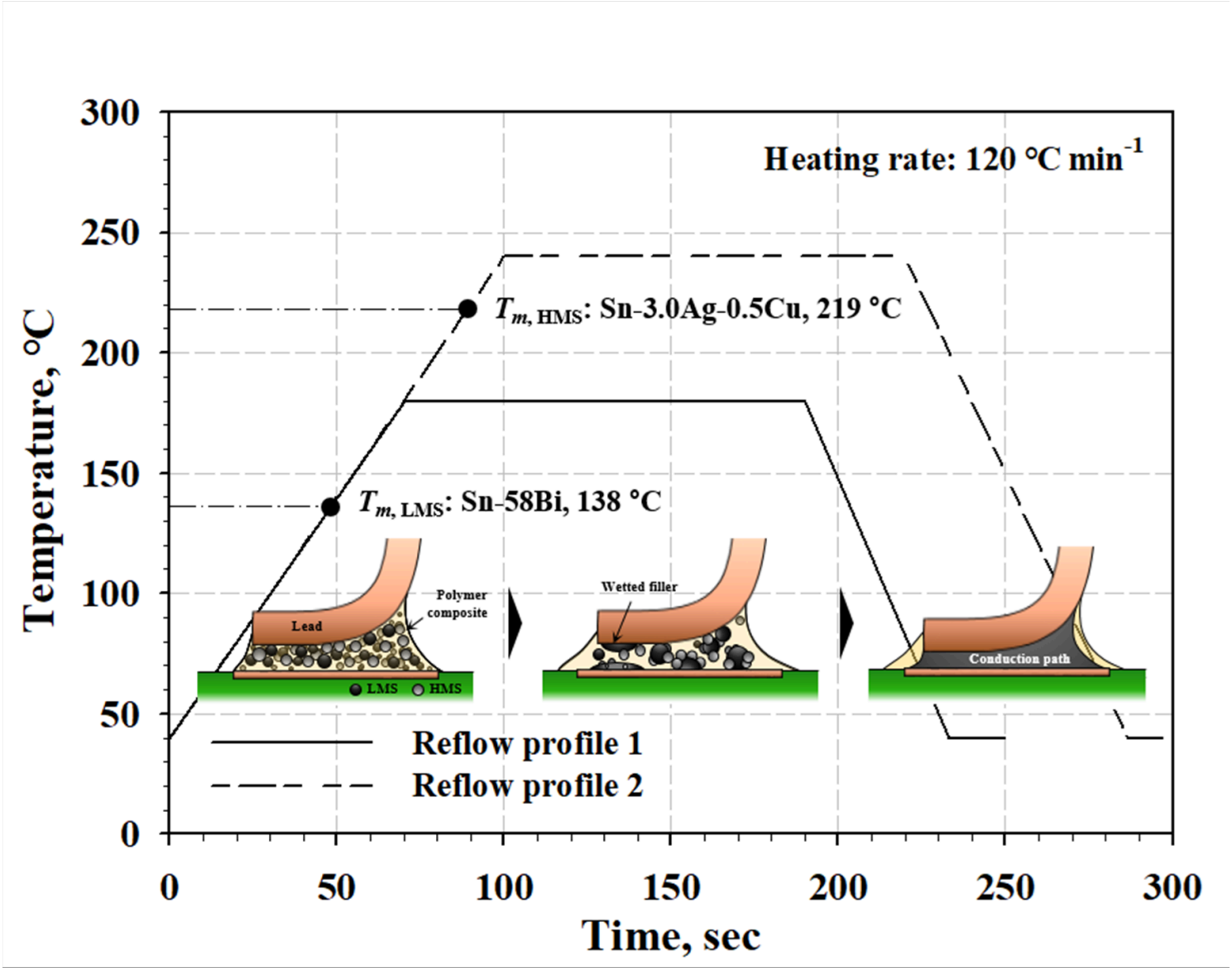


Figure 2

Reflow profiles for TQFP bonding with SAPCs.

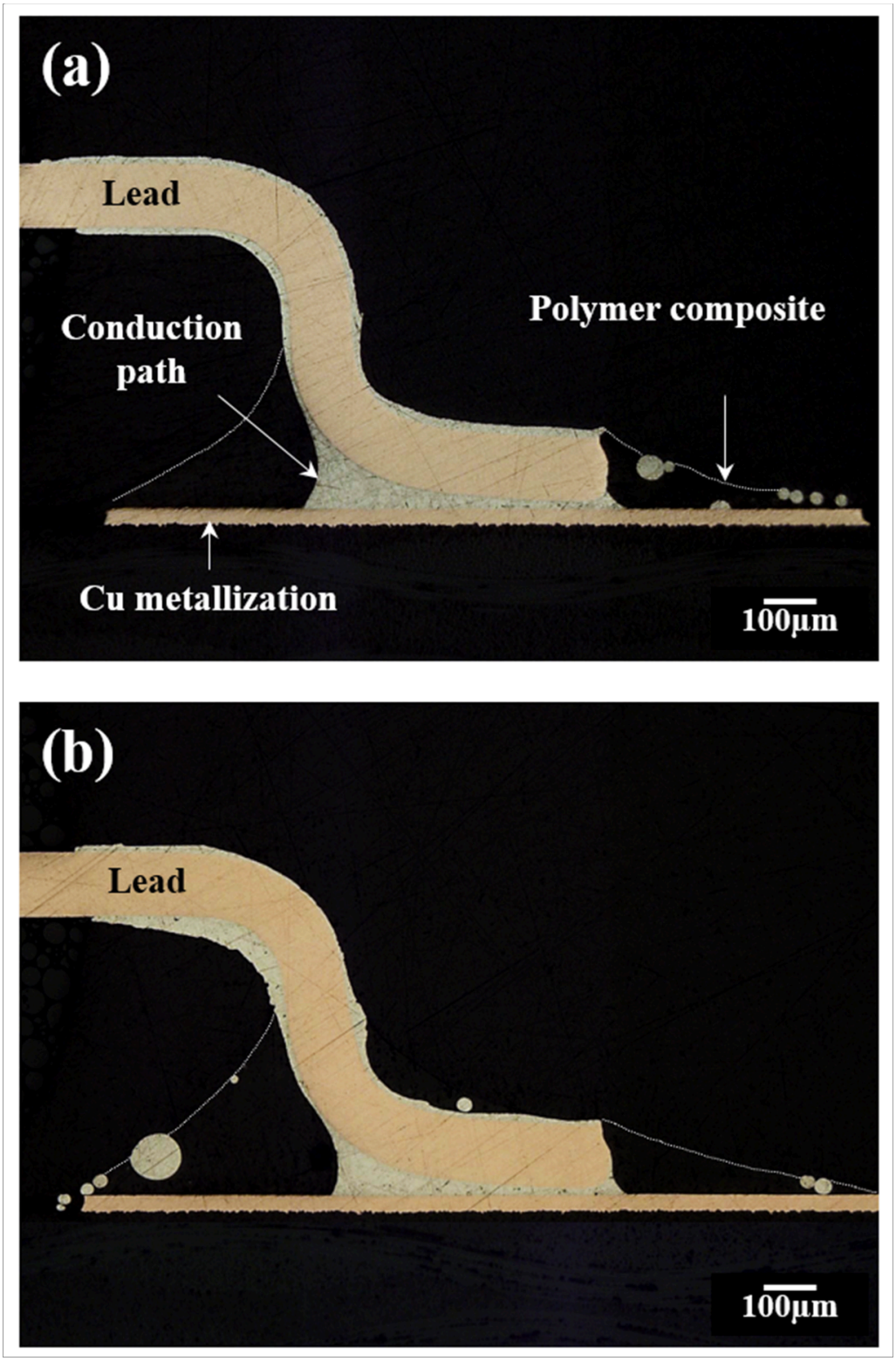


Figure 3

Cross-sectional conduction path morphologies before thermal shock testing for (a) L-SAPC (LMS only) and (b) LH-SAPC (LMS/HMS).

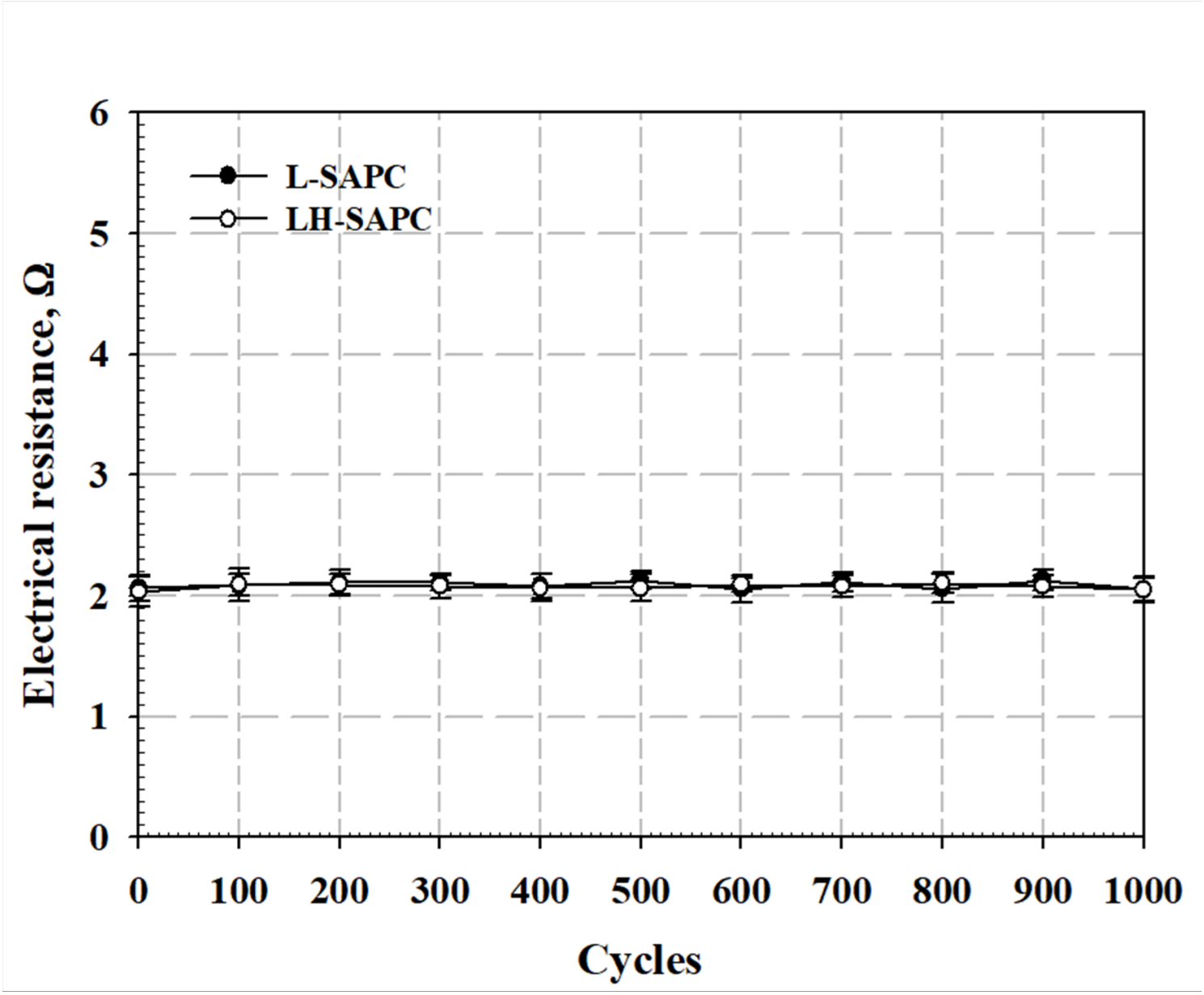


Figure 4

Electrical resistance changes in SAPC assemblies during thermal shock testing.

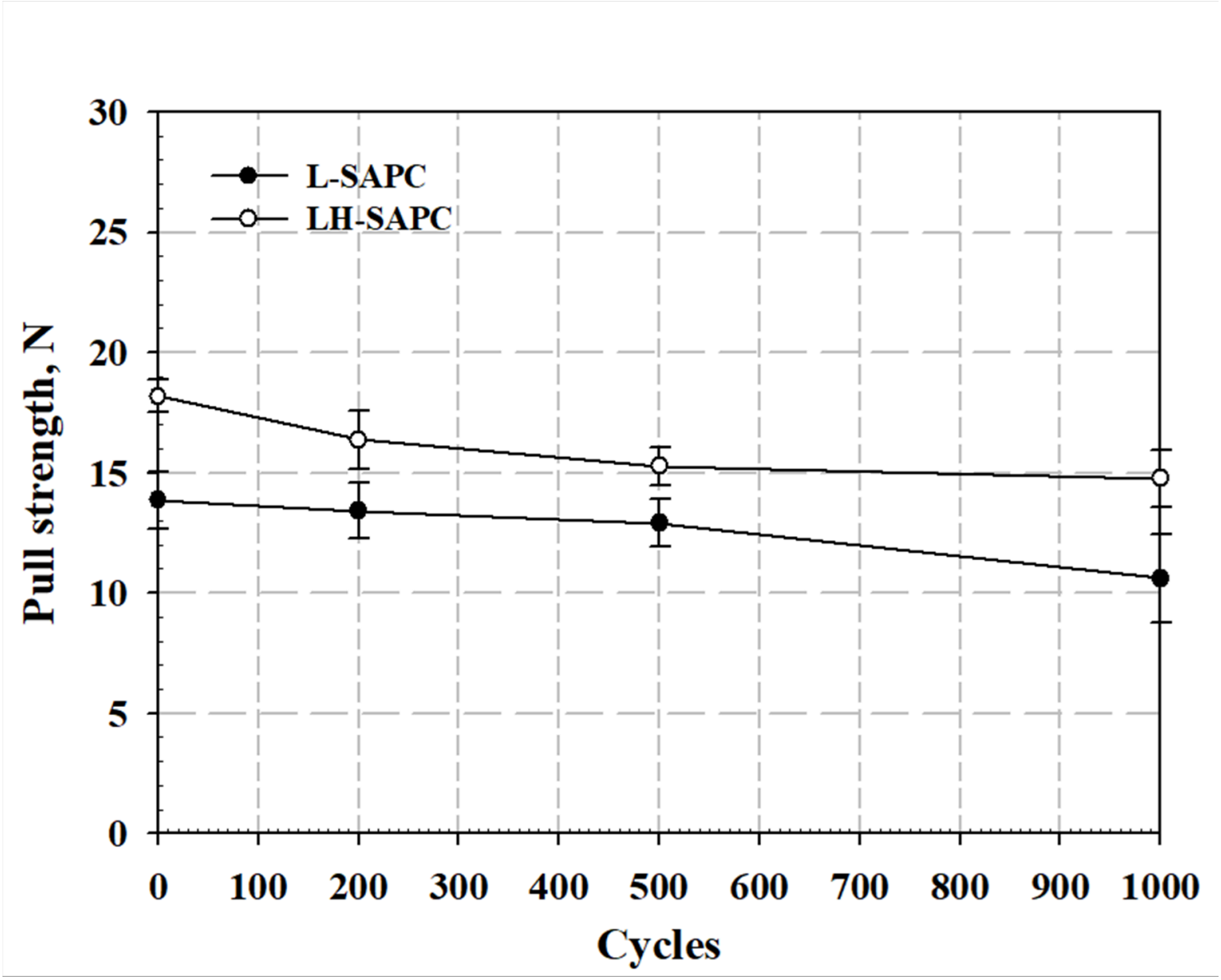


Figure 5

45°pull strength changes in SAPC assembly joints over thermal shock testing.

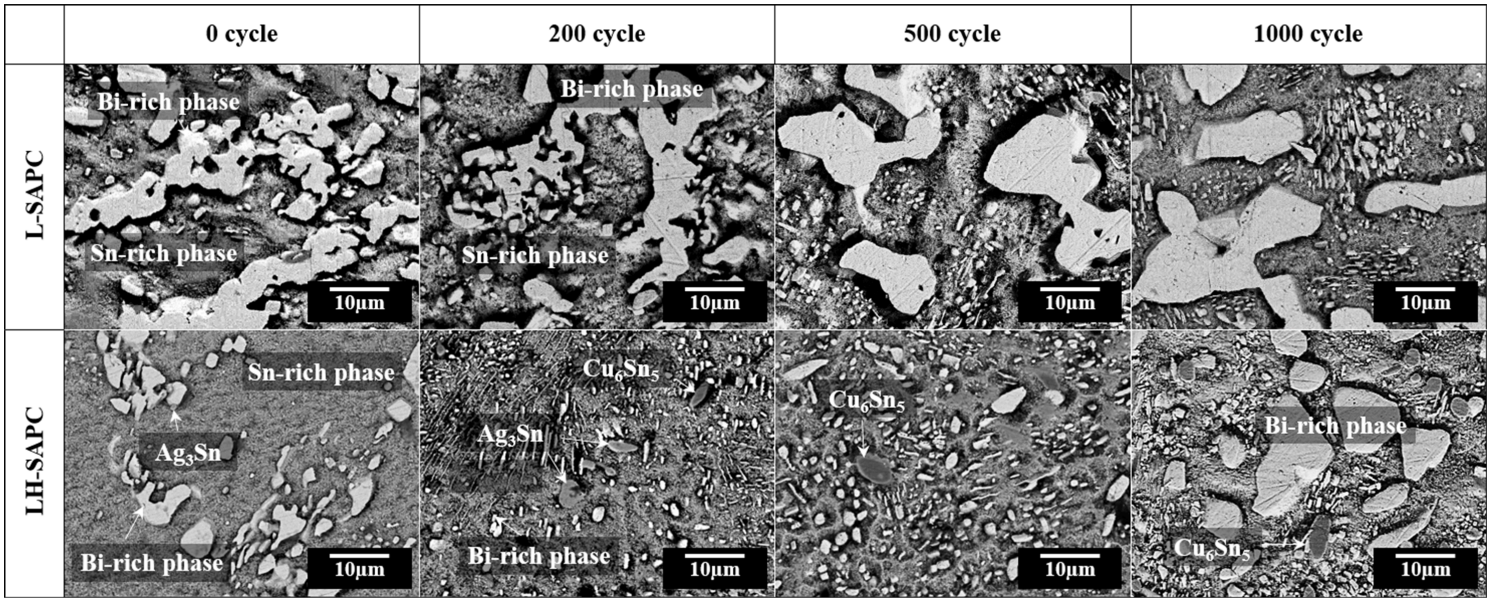


Figure 6

Microstructure in L-SAPC and LH-SAPC joints throughout thermal shock testing.

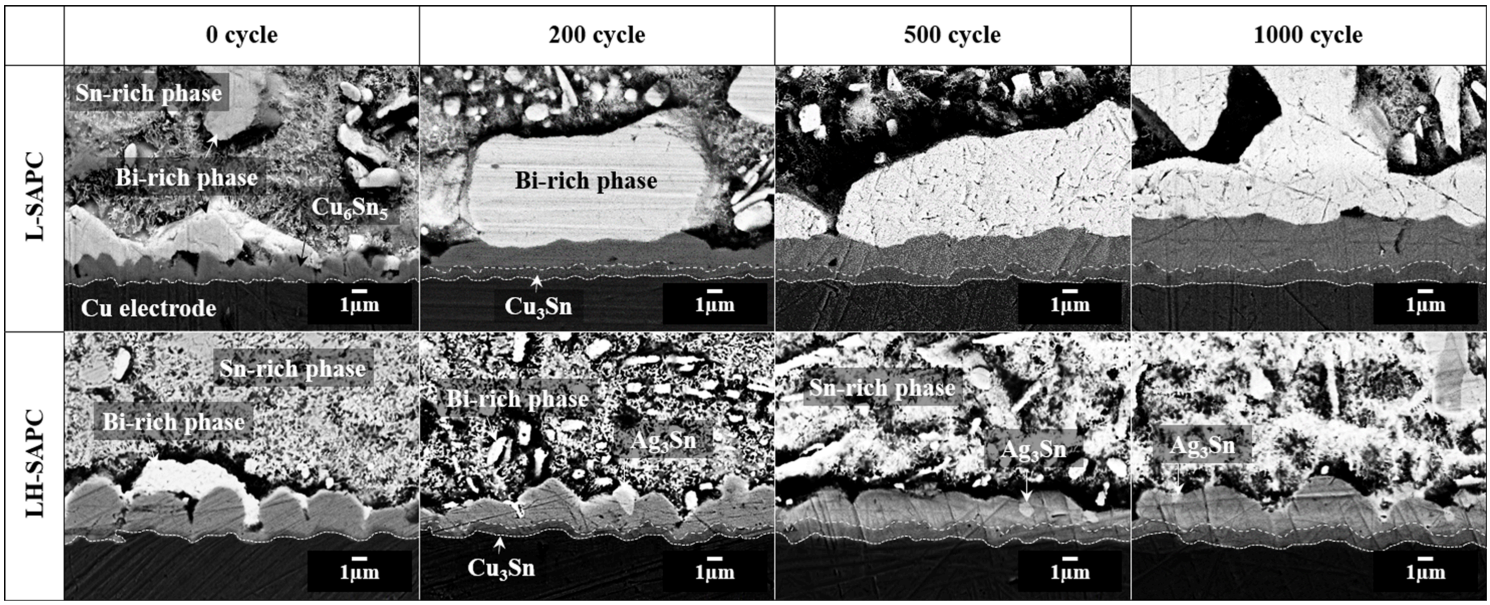


Figure 7

Interfacial IMC morphologies and thickness evolution in L-SAPC and LH-SAPC joints during thermal shock.

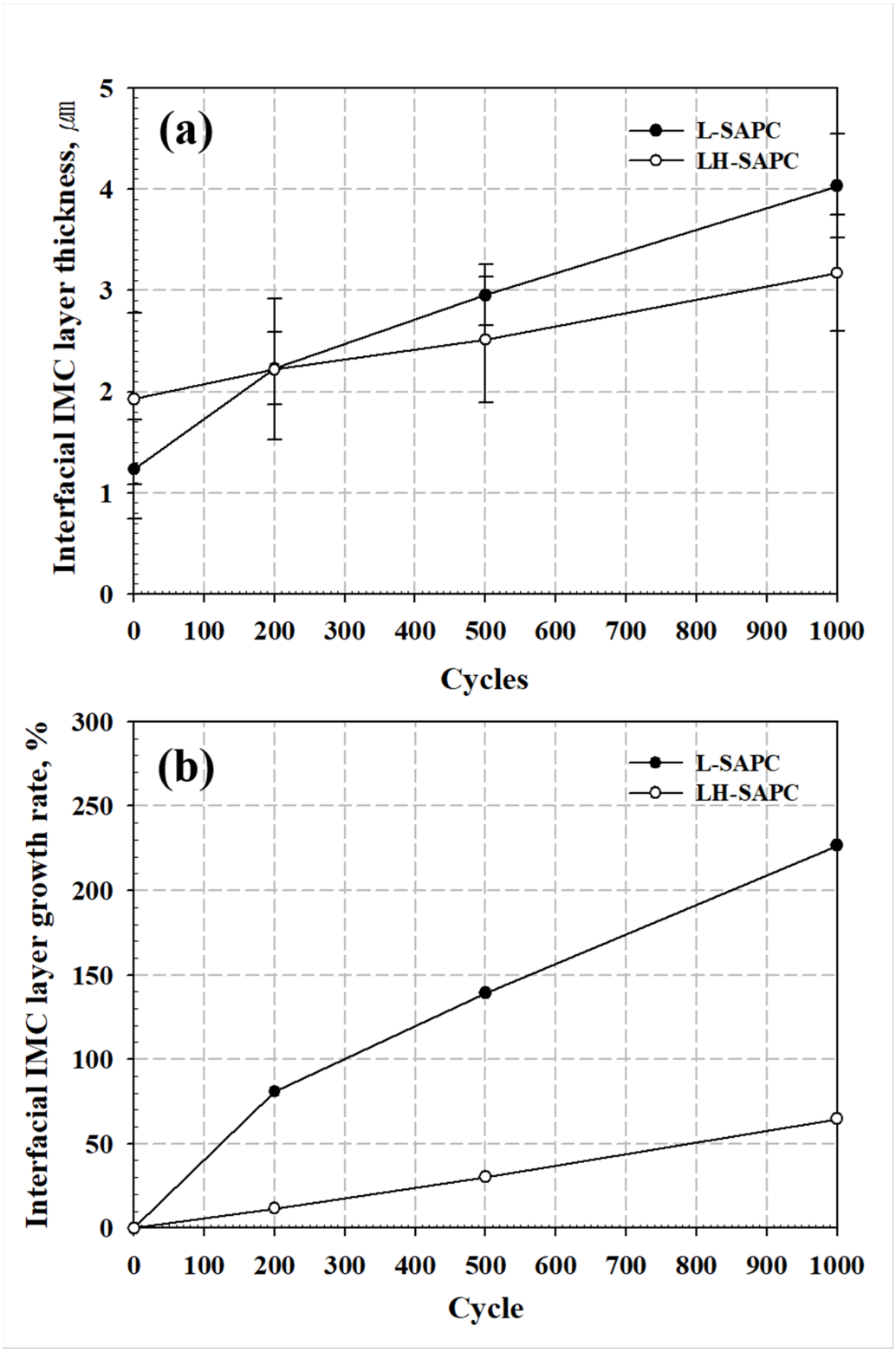


Figure 8

IMC layer (a) thickness and (b) growth rate variations of SAPC joints during thermal shock testing.

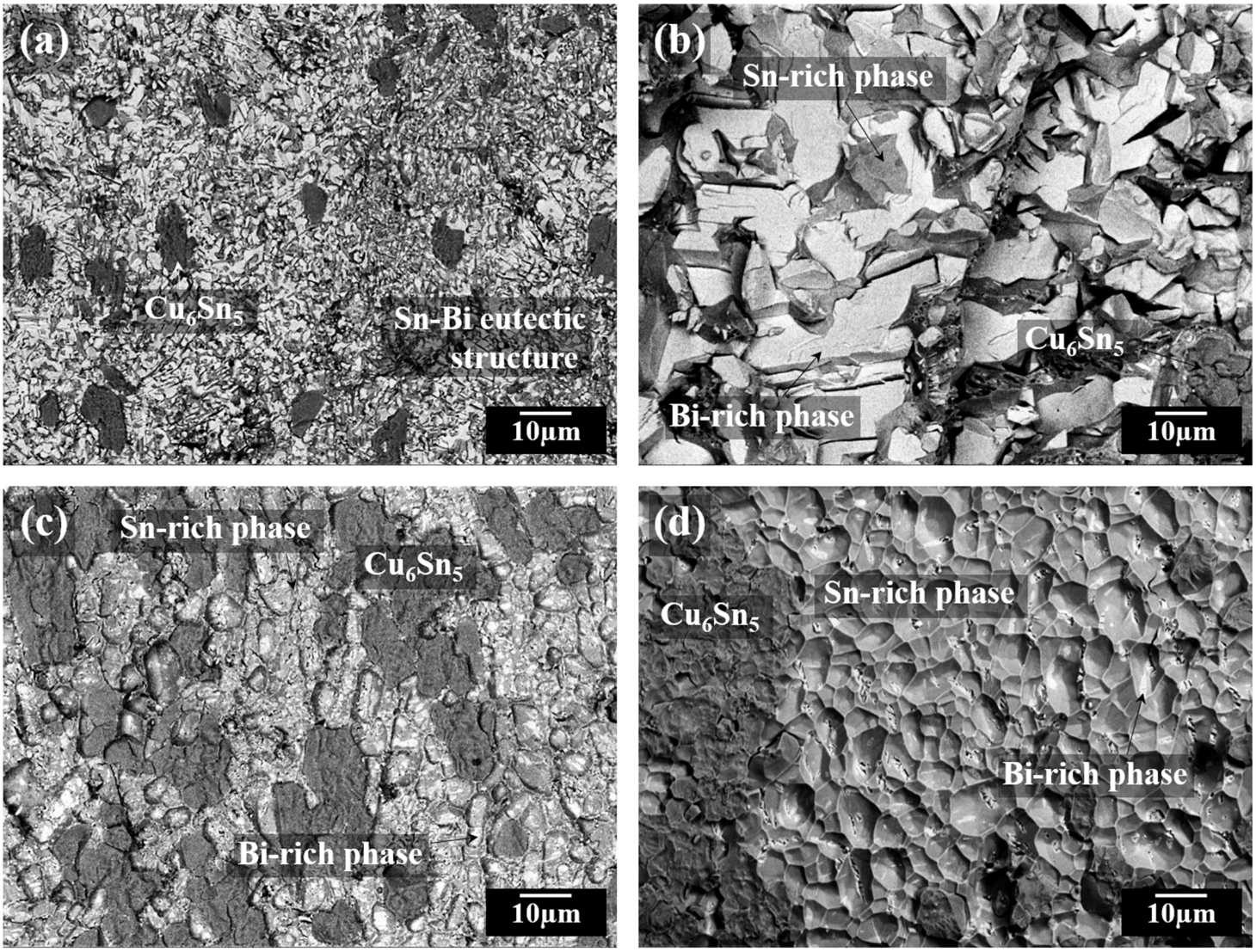


Figure 9

Fracture surface morphologies of L-SAPC joints (a) before and (b) after thermal shock, and LH-SAPC joints (c) before and (d) after thermal shock testing.